Bubbles Near a Vertical Wall: Experimental Investigation and Flow Analysis

R. Cai[1,2], J. Sun[1,2,3] and W. Chen[1,2†]

[1] *Department of Process Equipment and Control Engineering, Hebei University of Technology, Tianjin 300130, China*
[2] *National-Local Joint Engineering Laboratory for Energy Conservation in Chemical Process Integration and Resources Utilization, School of Chemical Engineering, Hebei University of Technology, Tianjin 300130, China*
[3] *Department of Mechanics, School of Mechanical Engineering, Tianjin University, Tianjin 300350, China*

†*Corresponding Author Email: cwy63@hebut.edu.cn*

ABSTRACT

The motion of bubbles near a solid vertical wall and the resulting induced flow field were experimentally investigated using the shadow method and particle image velocimetry (PIV). The study analyzed how bubble generation frequency and initial distance from the wall affect the average velocity distribution of bubbles and the characteristic parameters of the bubble-induced flow. The results demonstrate that a wall's presence can both decelerate and accelerate the movement of a bubble chain. This dual effect diminishes with increasing distance from the wall, and a higher bubble generation frequency can alleviate the slowing effect. The induced flow field near the wall generates secondary vortices, formed due to the wall's influence and the accumulation of leading-edge vortices from bubbles on the wall, especially at medium and low generation frequencies. However, at high generation frequencies, their formation is not solely attributable to these factors. Instead, it is primarily due to secondary induction within the bubble-induced flow, with the wall predominantly compressing the flow field. Additionally, proper orthogonal decomposition (POD) analysis reveals the impact of different bubble generation frequencies on induced flow characteristics. High-frequency bubbles exhibit a stronger flow-inducing capability, but in such cases, the subsequent bubble tends to disrupt the flow structure established by its predecessor, leading to a more uniform distribution of energy throughout the induced flow field.

1. INTRODUCTION

Amidst escalating environmental challenges and an energy crisis, carbon neutrality has gained significant attention as a key strategy to combat global climate change and mitigate greenhouse gas effects. Achieving zero net emissions entails balancing carbon dioxide (CO_2) emission and absorption. In this context, two-phase flow plays a crucial role, especially in refrigeration and heating systems. It effectively enhances energy transfer efficiency while concurrently reducing CO_2 emissions (Dai et al., 2024a, b, c).

Understanding the behavior of bubbles in close proximity to a wall and the resulting induced flow is crucial in engineering practice. Their influence on heat transfer efficiency, mass transfer, mixing, pressure drop, and other processes underscores the need for detailed investigation. Research has increasingly focused on this

area to comprehend the impact of bubbles near solid walls on flow dynamics (Jeong & Park, 2015; Métrailler et al., 2017; Gong et al., 2020; Yu et al., 2020; Zhang et al., 2020; Maeng & Park, 2021; Yin et al., 2021; Yuan et al., 2021; Yan et al., 2023).

The investigation of individual bubble behavior near a solid wall is currently a prominent focus in academic research. In the absence of a wall, an increase in the Reynolds number enhances bubble motion freedom. At low Reynolds numbers, bubbles typically ascend along a one-dimensional straight path. However, as the Reynolds number rises, the bubble gradually transitions into a two-dimensional zigzag trajectory and eventually evolves into three-dimensional spiral motion (de Vries, 2001; Zenit & Magnaudet, 2008; Zhang & Ni, 2017). The presence of a wall can impose constraints on bubble behavior and lead to unexpected outcomes. Depending on size and initial distance from the wall, a bubble may either bounce or

NOMENCLATURE			
L	initial distance	L^*	normalized initial distance
r_{eq}	equivalent bubble radius	V_b	bubble velocity
F	Frequency of bubble generation	d	distance from the average bubble position to the wall
x	x-axis coordinate	z	z-axis coordinate
ω	vorticity of the bubble induced flow	u	velocity of the bubble induced flow
H	height position in the flow field	$\overline{uu}$	Reynolds normal stress in the flow direction
$\overline{vv}$	Reynolds normal stress in the wall-normal direction	$\overline{uv}$	Reynolds shear stress
T	horizontal position in the flow field		

exhibit slip phenomena on the wall (de Vries et al., 2002). Simulation results (Zaruba et al., 2007) show that bubbles with Reynolds numbers ranging from 220 to 1000 exhibit constant magnitude bouncing motion. This phenomenon is believed to result from the mutual cancellation of two factors: the dampening effect from bubble-wall collisions and the additional energy induced by bubble shape oscillation. The primary manifestation of the wall's constraint effect on bubbles is in the direction of wall spreading. In the direction perpendicular to the wall, the presence of the wall enhances bubble motion (Zhang et al., 2020).

The properties of the wall are crucial factors influencing bubble behavior in close proximity to it. Conventional non-slip walls typically result in energy dissipation upon impact. The amplitude and wavelength of bubble motion decrease compared to free bubbles due to the presence of the wall, leading to higher energy dissipation. Energy dissipation near porous walls remains unaffected by initial distance. On hydrophobic surfaces, energy dissipation is directly proportional to initial distance, resulting in an upward sliding motion of the bubble along the surface (Jeong & Park, 2015). Additionally, the hydrophobic nature of the wall significantly influences bubble morphology and subsequently affects ascent dynamics (Khodayar & Davoudian, 2018). A recent study (Chen et al., 2021) reveals that manipulating the initial distance between wire mesh walls does not significantly impact bubble motion characteristics. However, this type of wall can induce interference, leading to lateral migration and significant speed fluctuations.

Modifying the wake structure corresponds to altering bubble behavior (Zhang & Ni, 2017). When a bubble approaches a wall, the wall's presence can intensify vortex shedding in the bubble's wake (Lee & Park, 2017; Yan et al., 2022). Furthermore, the wall constraint induces an asymmetrical distribution of the flow field surrounding the bubble, modifying the gas-liquid interaction and resulting in lateral migration of the bubble (Sugioka & Tsukada, 2015). The wall also impedes the dispersion of wake vortices generated by the bubble, inducing a repulsive force that propels the bubble away from its vicinity (Yan et al., 2023).

Under realistic conditions, isolated bubbles are rare; instead, multiple bubbles are more common. The velocity of the flow field induced by bubbles increases with the number of bubbles (Lee et al., 2021). When the frequency of bubble release is below 3 Hz, the bubbles follow consistent trajectories. However, when the frequency exceeds 4 Hz, bubbles exhibit erratic trajectory deviations attributed to liquid flow induced by neighboring bubble motion (Sanada et al., 2005). The rear bubble undergoes deformation and acceleration as it approaches the wake of the front bubble due to decreased resistance to inertia (Lee et al., 2021). Increased bubble frequency enhances the interaction between bubbles and liquid, intensifying the agitation effect on the flow. This disrupts the axisymmetric wake structure of the bubble, leading to lateral migration (Lee & Park, 2022).

To the best of our knowledge, most studies on bubbles in close proximity to walls have focused on individual bubbles. Further exploration is needed to understand bubble chain behavior near walls and the induced flow field characteristics, considering interactions between single and multiple bubbles. This study investigates the upward movement of bubble chains near a vertical wall and analyzes the resulting induced flow field. Data was collected using the shadow method and particle image velocimetry. Velocity distribution and induced flow field characteristics of bubbles are analyzed, considering the initial distance from the wall and frequency of bubble generation.

2. MATERIAL AND METHODS

The experimental setup is depicted in Fig. 1. Experiments took place in a rectangular plexiglass sink measuring 300 mm in length, 300 mm in width, and 650 mm in height. A stainless-steel needle, with an external diameter of 1.48 mm and an internal diameter of 1.12 mm, was positioned at the sink's center bottom. The wall, made of plexiglass, measures 580 mm in length, 200 mm in width, and has a thickness of 20 mm. The distance between the wall and the needle is precisely regulated by a lead screw, adjustable with an accuracy of up to 0.1 mm.

The continuous phase consists of a 35% glycerol aqueous solution. Table 1 presents the physical properties of this solution, while the liquid level in the tank remains consistently at a height of 450 mm. An air pump supplies constant pressure airflow, regulated further by a micro-regulating valve, generating a string of bubbles from the needle at various frequencies as outlined in Table 2. A CCD camera, operating at an acquisition frequency of 180 Hz and with a resolution of 2048×1280 pixels, captures the bubbles. LED lights illuminate the test area, with LED lights in the wavelength range of 320-350 nm employed to
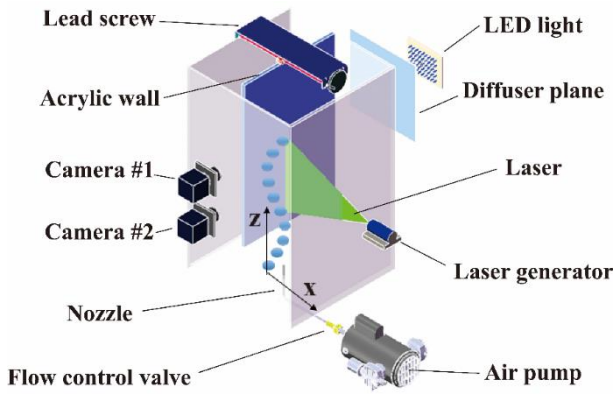
Fig. 1 Experimental setup showing two cameras simultaneously capture bubble movement and induced flow

Table 1 Solution properties at 20°C

Properties	Parameters
Density (kg/m^3)	1071.6
Viscosity (Pa s)	6.6×10^{-3}
Surface tension (N/m)	64.14×10^{-3}

Table 2 Bubble generation frequencies values set using the flow control valve shown in Fig. 1

Frequency	*F1*	*F2*	*F3*
Value (Hz)	5	16	38

mitigate the influence of background light, along with an appropriate filter placed in front of the camera. The installation of sulfate paper as a light diffuser between the light source and the sink ensures consistent illumination throughout, promoting uniformity.

The liquid velocity field induced by the bubbles was captured using the LaVision Particle Image Velocimetry (PIV) system. To mitigate the interference caused by light reflection from the bubble surfaces, PMMA particles coated with Rhodamine B were used as tracers. These tracers possess a nominal diameter of 2 μm and exhibit a density of 1.08 g/cm^3. The peak wavelength of fluorescent particle emission upon excitation with a green laser at 532 nm was measured to be approximately 618 nm. The laser beam was generated using a diode-pumped Nd: YAG laser (LPY700) capable of delivering a maximum energy output of 100 mJ. The Imager MX4M camera utilized in this experiment has a resolution of 2048x2048 pixels^2 and is equipped with a high-pass filter that effectively eliminates any strong reflections originating from the gas-liquid interfaces during imaging by setting its cut-off wavelength at 540 nm. Images were captured using a double-frame double-exposure method with a sampling frequency of 90 Hz. The results for each case were documented using 10,000 images.

Uncertainties in the experimental process encompass two primary aspects. First, an error is generated during the edge-detection process in bubble recognition (Celata et al., 2007). When the bubble does not collide with the wall, the maximum error in bubble edge recognition is ± 1 pixel,

Table 3 Normalized initial distance (needle-wall Separation)

| Initial distance	*L1*	*L2*	*L3*
L^*	0.5	1.5	3

resulting in a maximum uncertainty of less than 3% in the bubble diameter. However, when the bubble collides with the wall, this maximum error increases to ± 2 pixels and consequently leads to an uncertainty of less than 5% in the bubble diameter. Secondly, an error arises from the measurement of the velocity of the flow field induced by the bubbles. This measurement error can be attributed to factors such as the image resolution, image deformation, and acquisition frequency of high-speed cameras (Choi et al., 2019). Under current circumstances, it is estimated that this error remains below 3%.

The initial distance (L) was defined as the distance between the center of the needle and wall. It was normalized using the equivalent bubble radius (r_{eq}), and the calculation formula was $L^* = L/r_{eq}$, $r_{eq} = \sqrt[3]{d_h^2 d_v} / 2$, where d_h and d_v are the horizontal and vertical axes of the bubble, respectively. Based on the categorization of wall effect strength in previous studies (Jeong & Park, 2015; Lee & Park, 2017), three normalized initial distances were selected, and the corresponding parameters are presented in Table 3.

The original image was processed using the same methodology employed in our previous study (Cai et al., 2024), resulting in a contour image of the bubble along with the correlation characteristic parameters. Additionally, we obtained liquid-phase images that were free from the influence of bubbles, and finally acquired the liquid-phase velocity field. Based on the characteristic parameters of the bubble contour, such as the major and minor axes, area, roundness, and displacement between consecutive frames, we matched the bubble contour in adjacent images to achieve precise tracking. Consequently, we determined the kinematic characteristics of the bubble, including its speed and trajectory. Figure 2 depicts a segment of a time series illustrating the ascent of a chain of bubbles. The trajectory of the bubble is represented by the colored curve behind it, with distinct colors corresponding to the varying velocities.

3. RESULTS AND DISCUSSION

Bubble ascending sequence images of various frequencies were selected for computation, with 1000 pictures chosen for each frequency to acquire multiple complete bubble trajectories in close proximity to the wall. Superposition of bubble tracks with identical generation frequencies was conducted to acquire the distribution of tracks for bubbles with different frequencies near the wall, as illustrated in Fig. 3. As the frequency of the bubbles increased, certain trajectories demonstrated a more pronounced deviation from the wall. Additionally, there was an increase in the amplitude of the bubble trajectory, accompanied by a reduction in the inhibitory effect of the wall on the bubble velocity. In Fig. 3 (a) and 3 (b), the trajectory near the wall exhibits cyan and blue coloration,
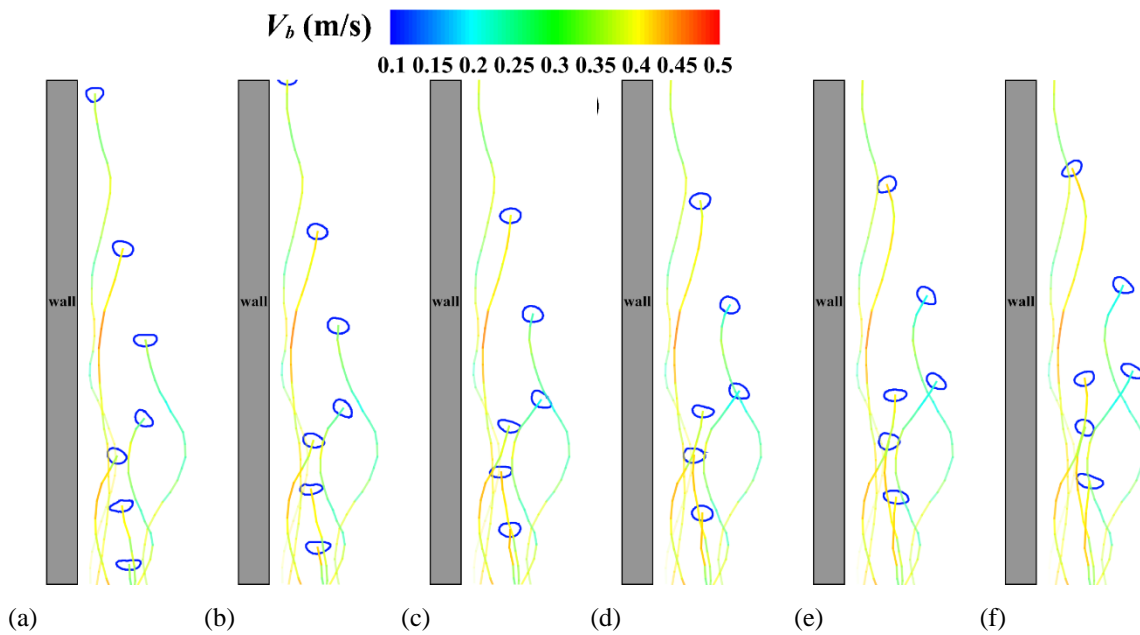
Fig. 2 Time series segment of bubble chain migration near the wall. (a) t = 55 ms; (b) t = 66 ms; (c) t = 77 ms; (d) t = 88 ms; (e) t = 99 ms; (f) t = 110 ms
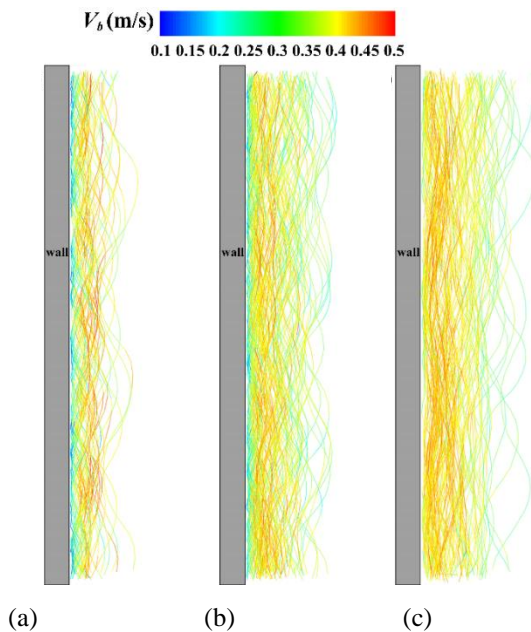
**Fig. 3 Bubble trajectory distribution at various frequencies near the wall; frequencies (a), (b), and (c) correspond to *F1*, *F2*, and *F3* respectively. Initial distance: *L1***

whereas the bubble velocity is approximately 0.15. This scenario is not shown in Fig. 3 (c). The collision between a single bubble and the wall is considered the primary factor contributing to the deceleration of the bubble velocity during migration near a solid boundary (Jeong & Park, 2015). However, in this study, we observed bubble wall collisions under various operational conditions. It is evident that collisions alone do not solely contribute to a reduction in bubble velocity. The increase in bubble frequency led to a decrease in wall suppression, thereby influencing the change in bubble velocity.

To quantify the influence of the wall on the bubble velocity, we obtained the corresponding relationship between the bubble velocity and distance from the wall by averaging the rising velocity of each bubble and its distance from the wall, as shown in Fig. 4. The horizontal coordinates represent the distance of the bubble from the wall, and the vertical coordinates denote its velocity. The presence of a wall generally leads to deceleration of the motion of an individual bubble (Krishna et al., 1999). The results for the bubble chain at various initial distances are presented in Fig. 4 (a), where the frequency of the bubbles is denoted by *F1*. The average velocity of the bubble demonstrated a consistent trend when the frequency remained constant and exhibited a positive correlation with the distance from the wall. When the wall distance exceeded a certain threshold, the velocity reached a stable state. The stable velocity value did not exhibit any significant variation for different initial distances; however, for larger initial distances, bubbles emerged at greater distances from the wall.

For small wall distances ($d < 4$), the velocity of the bubbles near the wall decreases as the distance from the wall decreases, whereas it gradually increases with increasing wall distance. This consistent trend was observed irrespective of the bubble generation frequency, as shown in Fig. 4 (b), for an initial wall distance of *L1*. The noteworthy observation is that, despite the increase in bubble frequency, the bubble velocity does not consistently exhibit a fixed trend like *F1*. In the case of *F2*, when $d = 4$, the average bubble velocity tended to stabilize; however, when $d > 10$, there was a slight decrease in the average bubble velocity. When the bubble frequency reached *F3*, the stabilization phase terminated rapidly, and the average bubble velocity exhibited an earlier and more pronounced decrease. This phenomenon is attributed to the gas-liquid coupling effect. Bubbles with higher generation frequencies possess enhanced inducing

(a) (b)
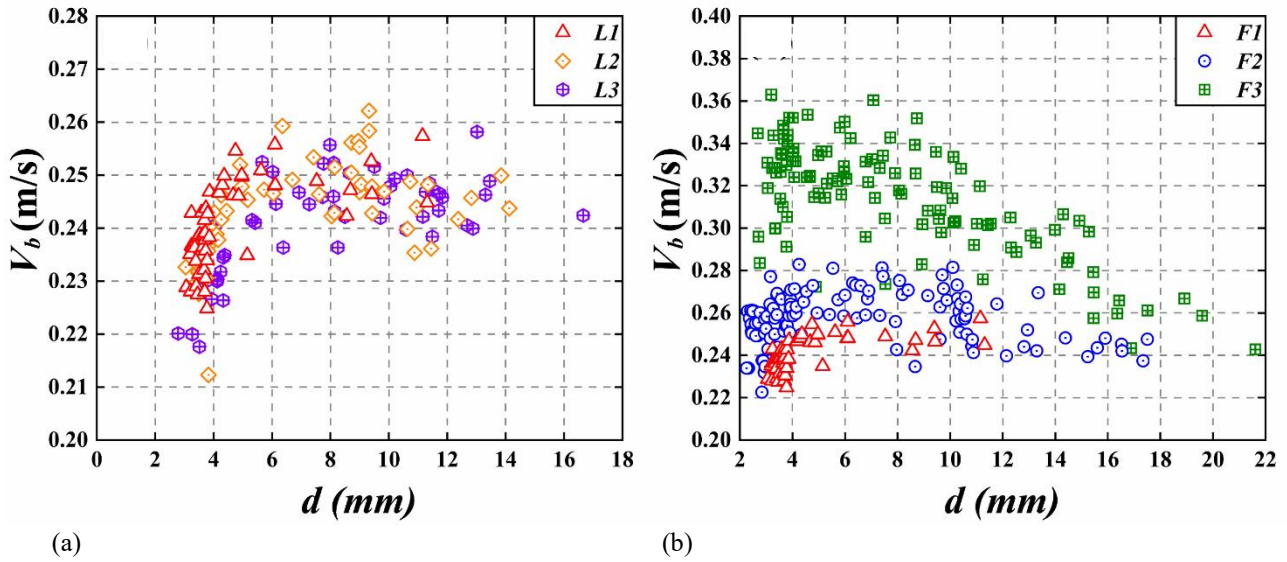
Fig. 4 Distribution of average bubble velocities. Here *d* represents the distance between the average position of the bubbles, corresponding to their average velocity, and the wall. (a) Impact of initial distance; (b) Influence of bubble generation frequency

capabilities; however, bubbles located in the mainstream region of the induced flow field experience reduced resistance. Consequently, the bubble-induced flow facilitates the bubble motion, which is consistent with the findings reported by Lee et al. (Lee et al., 2021). However, in the mainstream region, the liquid-phase velocity decreases, and the resistance of the bubble increases, resulting in a more rapid decay of bubble velocity.

The ascending sequence of the bubble chain adjacent to the wall and instantaneous vorticity field generated by these bubbles are illustrated in Fig. 5. The symbol ω denotes the vorticity of the flow field induced by bubbles, and its calculation formula is as:

$$\omega=\frac{1}{2}\left(\frac{\partial u}{\partial x}-\frac{\partial v}{\partial z}\right). \tag{1}$$

The directional orientation of each bubble is indicated by arrows. The vorticity and the corresponding position coordinates were normalized using the bubble's equivalent radius (r_{eq}) and velocity (V_b). For a single bubble ascending in a zigzag or spiral trajectory, a typical wake structure comprises a pair of counter-rotating vortices trailing behind the bubble. Alterations in the path of the bubble are associated with changes in the vortex configuration (Mougin & Magnaudet, 2002; Zenit & Magnaudet, 2008). When approaching the wall, a leading-edge vortex is induced by the compression of the wall and rotation of the bubble. In addition, the thin vorticity layer is similar to the boundary layer formed on a wall (Lee & Park, 2017). The flow field induced by the bubble chain is similar to that of a single bubble, with the presence of a reverse vortex and a leading-edge vortex observable in the wake. However, the vortex induced by the bubble chain persists for a longer duration. The vorticity layers resembling the boundary layer adjacent to the wall demonstrated an increased thickness and persisted continuously. This is attributed to the continuity of the flow field induced by the chain of bubbles, wherein the

energy loss in the wake of each preceding bubble is compensated for by the induction from subsequent bubbles.

The normalized average bubble-induced vorticity field is shown in Fig. 6 (a)–(c) illustrate the mean vorticity fields induced by bubbles of different frequencies at the same initial distance (*L1*). Figure 6 (c)–(e) show the average vorticity field induced by bubbles at different initial distances but with the same generation frequency (*F1*). Figure 6 (f) shows the average bubble-induced vorticity field when the bubble frequency was *F1* and there was no wall. The absence of a wall can result in a distinct symmetry in the flow field induced by the bubble motion (Li et al., 2021), which can also be observed in Fig. 6 (f). After the addition of the wall, the flow field adjacent to it underwent compression, whereas there was no obvious change in the structure of the flow field away from the wall. As the initial wall distance decreased, a secondary vortex was observed near the top of the wall when the initial wall distance was *L1*, as shown in Fig. 6 (c). Increasing the generation frequency, as shown in Fig. 6 (b), led to the appearance of a secondary vortex at a lower height. Furthermore, with a further increase in the bubble generation frequency to *F3*, reverse vortex pairs emerged at distant positions from the walls. The appearance of a secondary vortex near the wall at this time was not solely attributed to the wall effect. The presence of a wall predominantly influenced the compression of the flow field.

The velocity distribution of the average flow field induced by the bubbles is shown in Fig. 7. It was normalized by the equivalent radius of the bubbles and the average velocity, with u_x representing the velocity component along the x-axis and uz representing the velocity component along the z-axis. In Fig. 7 (a) and (b), *H1*, *H2*, and *H3* correspond to different height positions in the flow field, as listed in Table 4. In this case, the bubble is generated at a frequency of F1 and has an initial distance of *L1*. In proximity to the wall ($x/r_{eq} < 1$), an increase in
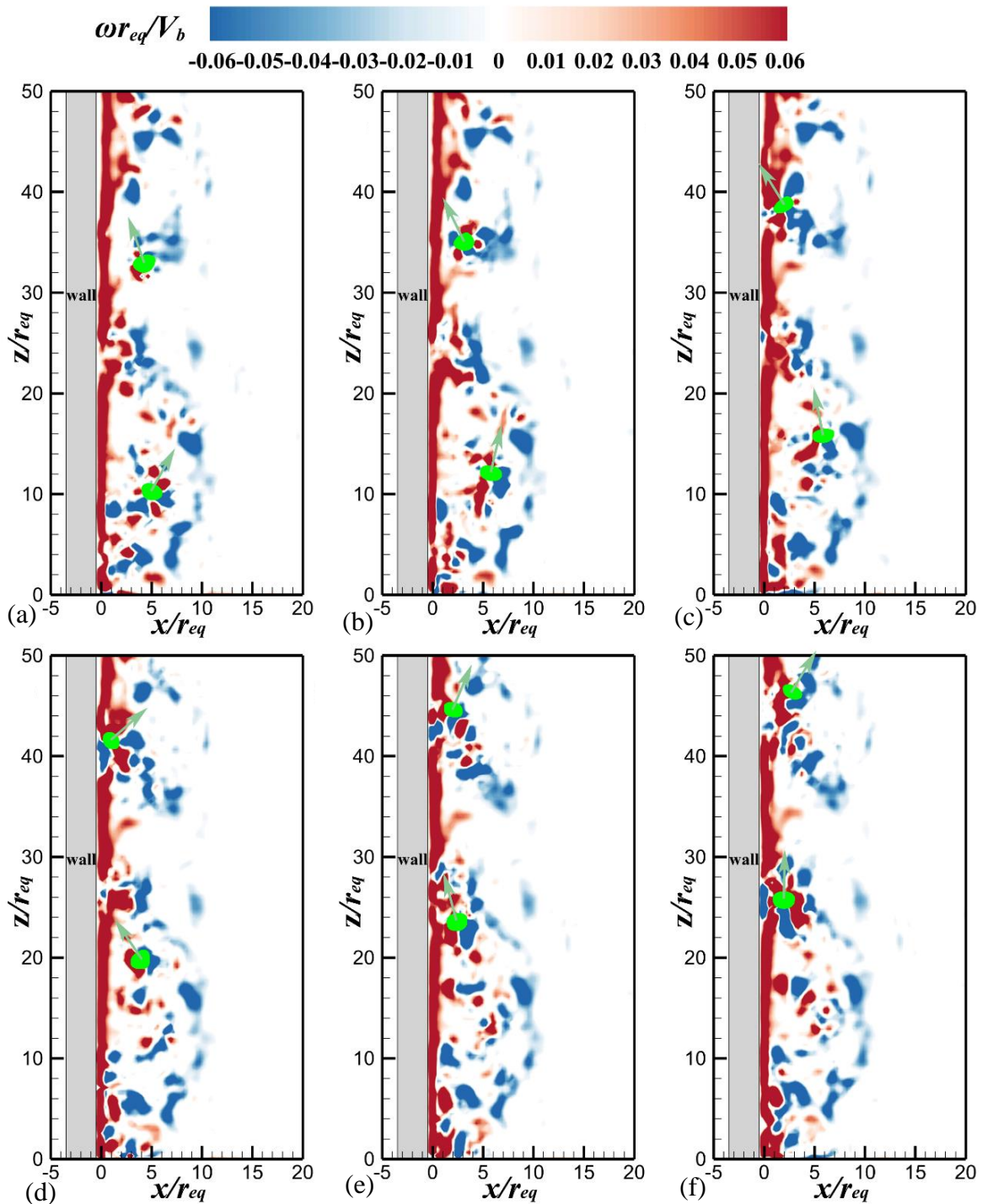
Fig. 5 Bubbles in the near-wall instantaneous vorticity field. (a) t = 110 ms; (b) t = 121 ms; (c) t = 132 ms; (d) t = 176 ms; (e) t = 187 ms; (f) t = 198 ms

the height resulted in a slightly higher $u_x/\bar{u}_x$ for $H2$ than for $H1$. However, there is a significant decrease in $u_x/\bar{u}_x$ with a further increase in height up to $H3$ owing to the emergence of a secondary flow. As x/r_{eq} increased, $u_x/\bar{u}_x$ gradually decreased until it reached a minimum at $x/r_{eq} = 0$. Subsequently, as x/r_{eq} continued to increase, $u_x/\bar{u}_x$ increased until it reached its peak value. Beyond this point, there tends to be a stable value with intermittent unstable fluctuations that signify weakening of the wall effect.

The distribution of $u_z/\bar{u}_z$ along the x-axis exhibits a more pronounced regularity than that of $u_x/\bar{u}_x$. $u_z/\bar{u}_z$ increased as the distance from the wall increased, reaching its peak at $x/r_{eq} = 2$ and gradually decreasing until it approached zero after $x/r_{eq} > 22$. Prior to reaching its peak, $u_z/\bar{u}_z$ followed a similar trend as height increased. In close proximity to the wall, $u_z/\bar{u}_z$ increased slightly with height. These findings suggest that as the bubble-induced flow field developed, the inhibitory effect of the wall on the flow velocity diminished to some extent.
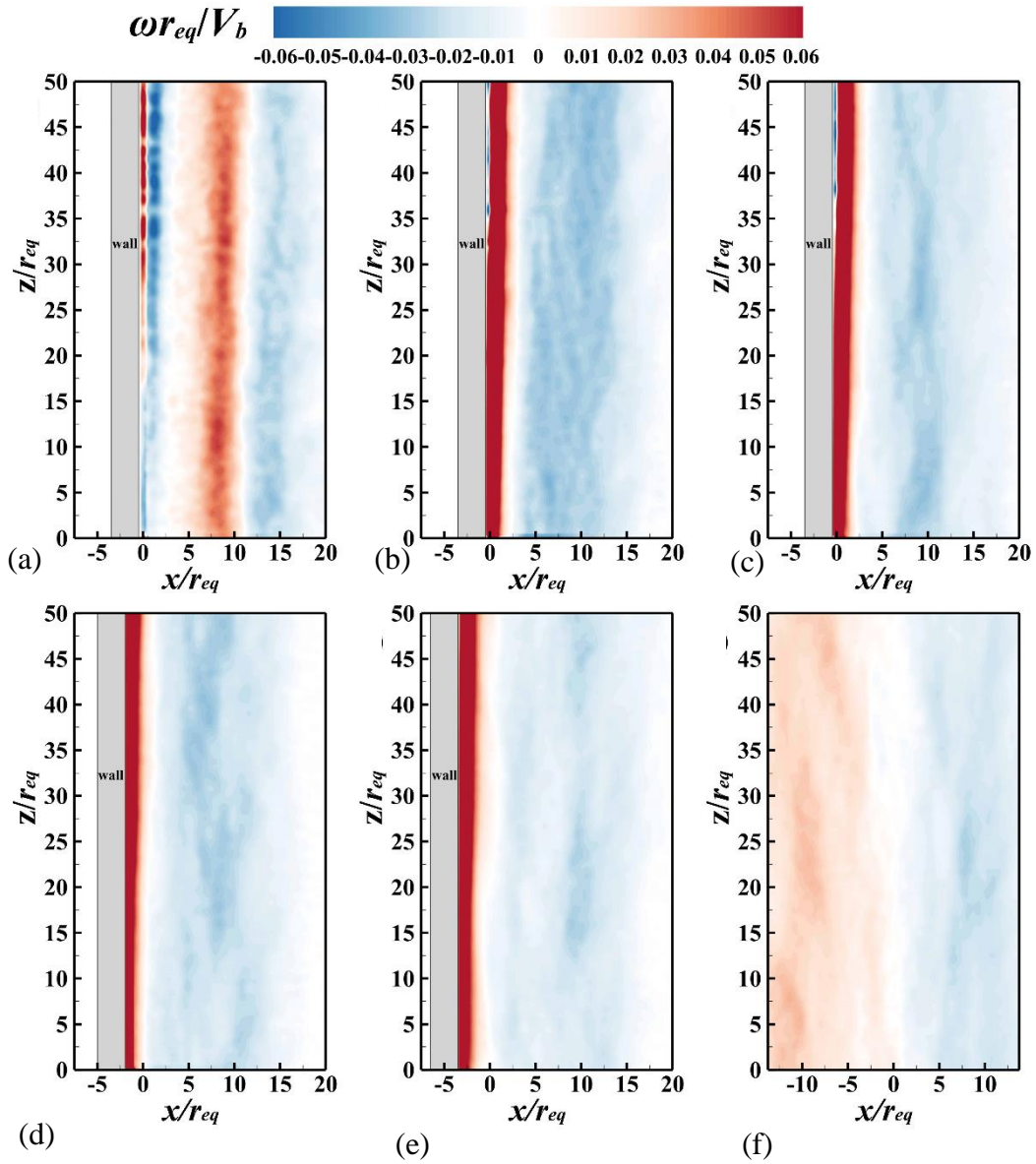
Fig. 6 Normalized average vorticity field induced by bubbles. (a) *L1, F3*; (b) *L1, F2*; (c) *L1, F1*; (d) *L2, F1*; (e) *L3, F1*; (f) *F1*, without wall

Table 4 Vertical position within the bubble-induced flow field

Position	$H1$	$H2$	$H3$
z/r_{eq}	15	30	45

Variations in the average velocity distribution of the bubble-induced flow field with different bubble generation frequencies are illustrated in Fig. 7 (c) and (d). The height of the flow field is $H2$, and the initial distance from the wall is $L1$. The effect of the wall on the average velocity of the bubble-induced flow field remained consistent across varying bubble frequencies. As x/r_{eq} increased, there was a gradual reduction in wall effects. Initially, $u_x/\overline{u}_x$ decreased, followed by an increase before exhibiting random fluctuations after reaching its peak value. $u_z/\overline{u}_z$ initially increases to its maximum value,

subsequently decreases, and eventually approaches zero. When comparing $F1$ to $F2$ in terms of the bubble frequency, a slight increment is observed in $u_x/\overline{u}_x$ whereas $u_z/\overline{u}_z$ becomes more similar. In comparison to $F1$, the near-wall values for $u_z/\overline{u}_z$ are smaller for $F2$ but larger at its peak position. When the frequency was increased to $F3$, a noticeable difference was observed in the velocity distribution. There was no significant change in $u_x/\overline{u}_x$ when $x/r_{eq} < 2$. However, when $x/r_{eq} > 2$, $u_x/\overline{u}_x$ gradually increases with increasing distance from the wall until it reaches its peak value. Compared to the other frequencies, $u_x/\overline{u}_x$ exhibited less fluctuation near the peak at frequency F1. Regarding $u_z/\overline{u}_z$, it initially decreases to a minimum value and then increases before decreasing again after reaching its peak value until it eventually approaches zero.
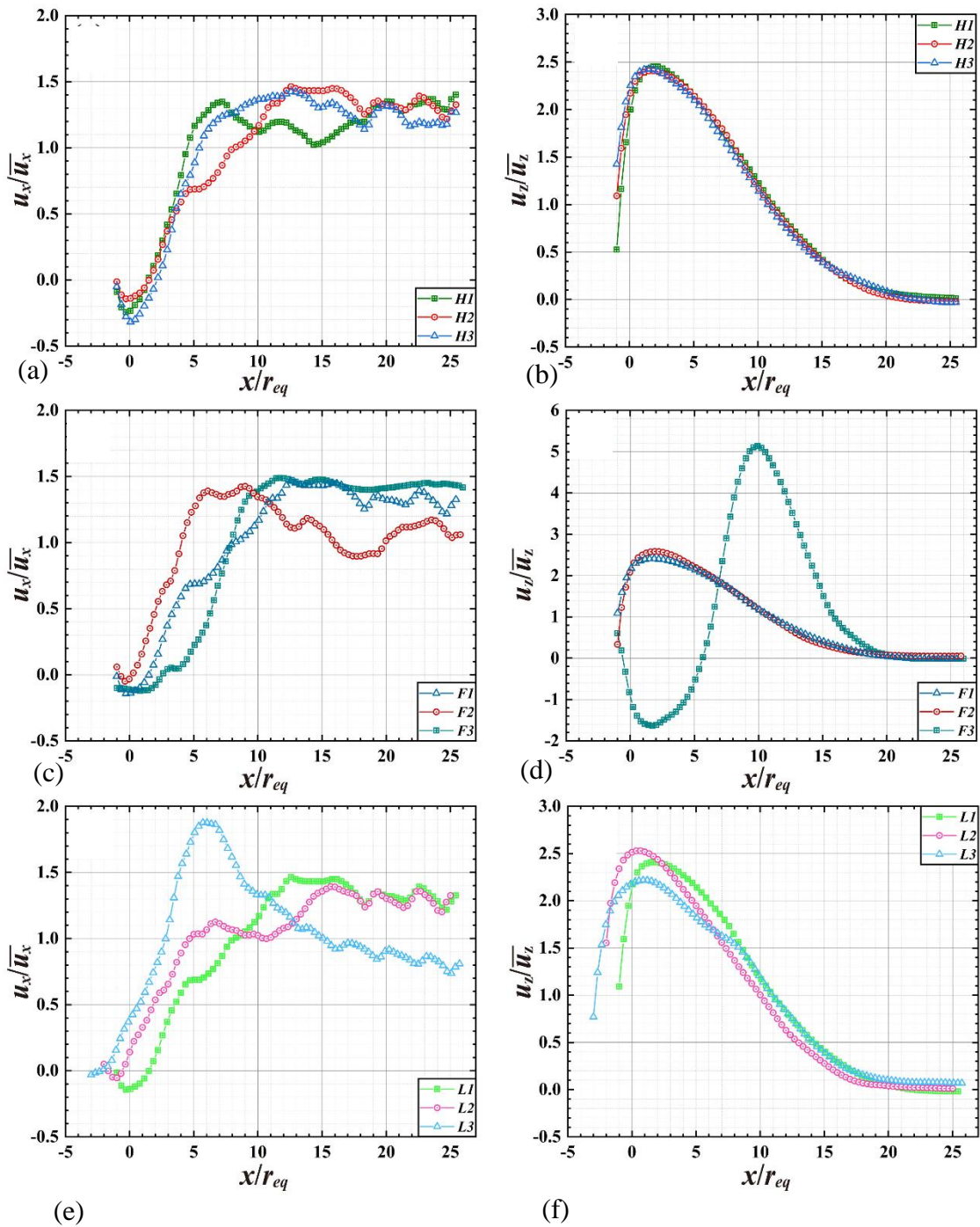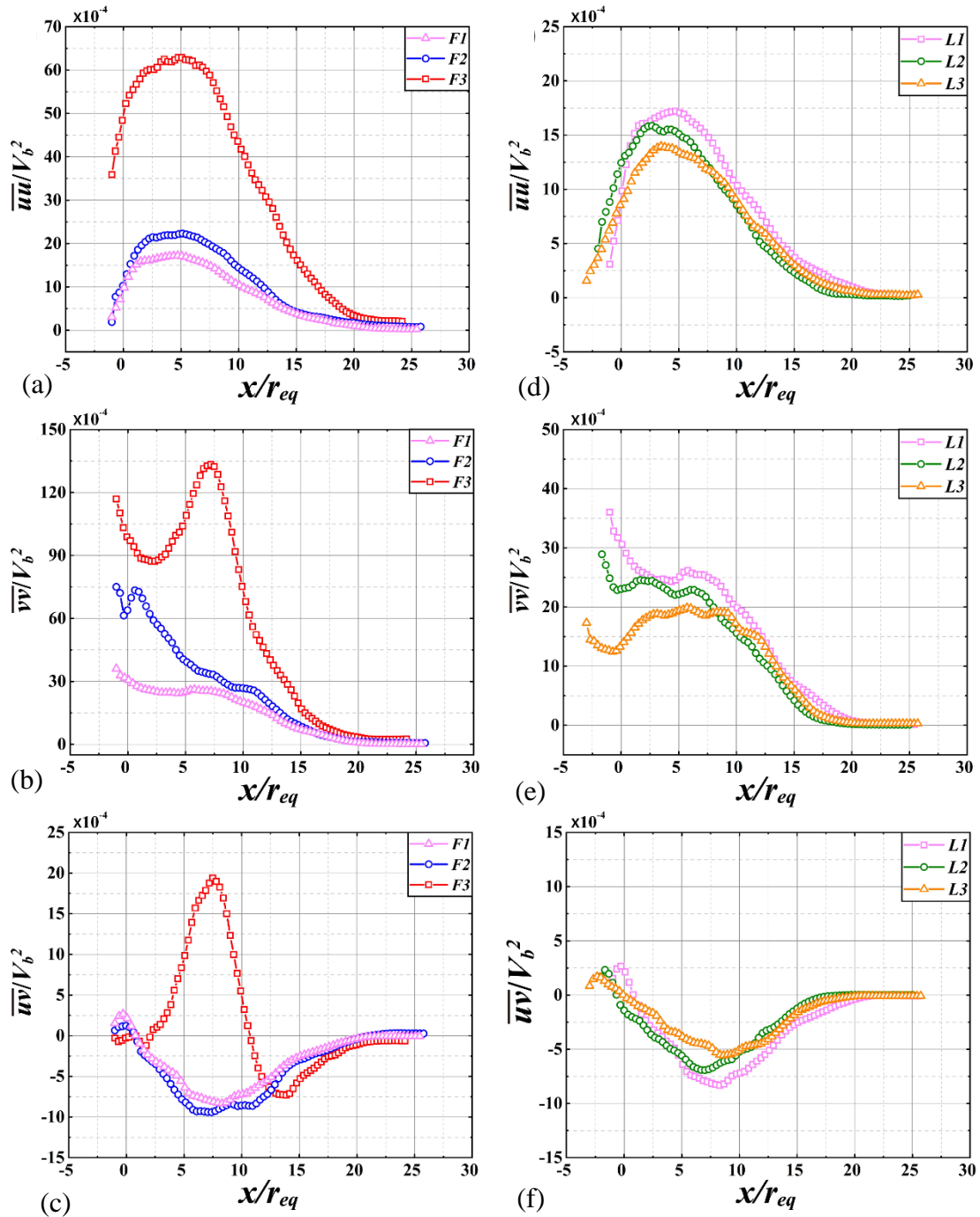
Fig.7 Average velocity distribution of the bubble-induced flow. (a) Influence of *H* on $u_x/\overline{u}_x$; (b) Influence of *H* on $u_z/\overline{u}_z$; (c) Influence of *F* on $u_x/\overline{u}_x$; (d) Influence of *F* on $u_z/\overline{u}_z$; (e) Influence of *L* on $u_x/\overline{u}_x$; (f) Influence of *L* on $u_z/\overline{u}_z$

This phenomenon was attributed to the presence of secondary vortices. Considering the distribution of the average vorticity field in Fig. 6, we observe that bubbles of different frequencies induce secondary vorticities in the flow fields owing to different factors. The generation of secondary vortices in low- and medium-frequency bubbles resembles that of single bubbles and primarily occurs because of wall shear and the accumulation of leading-edge vortices on the wall. However, the secondary vortices of the high-frequency bubbles primarily arise from the re-induction of the flow induced by the bubbles, while the main function of the wall is to compress and confine. As

bubbles traverse the flow field, the viscosity-induced shear generates a pair of counter-rotating vortices at the tail of the bubble. In close proximity to the wall, these vortices exhibited a counterclockwise rotation, resulting in velocity maxima along the positive z-axis within the flow field. This phenomenon is illustrated in Fig. 7(d) for x/r_{eq} = 10. Notably, a discernible decrease in velocity was observed on either side of the peak-velocity region. In addition, secondary vortices rotating in the opposite direction contributed to the formation of a velocity maximum along the negative z-axis direction, particularly at x/r_{eq} = 2. The sign of the velocity indicates the direction

Fig. 8 Distribution of Reynolds stress under different frequencies of bubble generation and varying initial distances. (a) Influence of F on $\overline{uu}/V_b^2$; (b) Influence of F on $\overline{vv}/V_b^2$; (c) Influence of F on $\overline{uv}/V_b^2$; (d) Influence of L on $\overline{uu}/V_b^2$; (e) $\overline{vv}/V_b^2$; (f) $\overline{uv}/V_b^2$

of fluid movement, while acknowledging that near-wall proximity intensifies its decay owing to shear effects.

The change in the average velocity distribution within the bubble-induced flow field as a function of the initial wall distance is illustrated in Fig. 7 (e) and (f). The height is $H2$ and the bubble frequency is $F1$. A consistent pattern of velocity component distribution with respect to x/r_{eq} was observed for different initial wall distances. Specifically, $u_x/\overline{u}_x$ initially decreases and then increases before fluctuating after reaching a peak. In contrast, $u_z/\overline{u}_z$

exhibits an increasing trend until it reaches its maximum value and subsequently decreases to zero. As the initial wall distance increased, $u_x/\overline{u}_x$ increased and reached its peak earlier, indicating a weakening of the wall effect.

In particular, when the initial wall distance is $L3$, $u_x/\overline{u}_x$ exhibits a direct increase near the wall without adhering to the conventional pattern of first decreasing and then increasing. This observation suggests that the influence of the wall alone is insufficient to generate a secondary vorticity. As mentioned previously, the wall effect

decreased as the initial wall distance increased. Consequently, *L2* has a smaller peak of $u_z/\overline{u_z}$ compared to *L1*. However, *L3* had an even smaller $u_z/\overline{u_z}$ peak than both *L1* and *L2*. These findings suggest that the wall has effects beyond those of inhibition. The presence of the wall, which can compress the flow field, promotes an increase in the flow velocity by considering the Bernoulli effect. Notably, *L2* demonstrated the highest peak flow velocity owing to a combination of inhibitory and promoting effects from the wall. When the initial wall distance was set at *L3*, neither the inhibitory nor promoting effects were significant. With an initial distance of *L2*, there is a significantly enhanced promoting effect from the wall but still no dominant inhibiting effect observed. Conversely, when the initial distance was *L1*, the inhibition and promoting effects were evident. Therefore, the velocity of the flow at *L1* was intermediate between those at *L2* and *L3*.

Considering the similarity of the Reynolds stress at different heights in the flow field, we compared the effects of the initial wall distance and bubble frequency on the distribution of the Reynolds stress, as shown in Fig. 8. The height of the flow field is *H2*, the initial distance in Fig. 8 (a)–(c) is *L1*, and the frequency of bubble generation in Fig. 8 (d)–(f) is *F1*. Wang's study on bubble-induced flow fields in a free-flow environment demonstrates that the distribution of Reynolds normal stress along the x-axis remains symmetric when there is no wall effect, which holds true for both $\overline{uu}$ and $\overline{vv}$ components (Wang & Socolofsky, 2019). For regions located away from the wall, the distribution pattern of $\overline{uu}$ was similar to that induced by an unconfined bubble, particularly on the right side, relative to the symmetry axis in the absence of a wall.

However, the Reynolds stress in the near-wall regions exhibited an amplified growth rate owing to the influence of the wall, reaching its peak at x/r_{eq} = 5. The position of the maximum $\overline{uu}$ in the bubble-induced flow fields remained consistent across different frequencies. As the frequency increased, the magnitude of the maximum value also increased. Furthermore, reducing the initial wall distance increased the peak value of $\overline{uu}$, as shown in Figs. 8 (a) and (d). These findings suggest that both intensified wall effects and increased bubble frequencies can augment the induction ability of bubbles in the flow direction.

The $\overline{vv}$ distributions under different bubble frequencies and initial wall distances are shown in Figs. 8 (b) and (e), respectively. Similar to $\overline{uu}$, an increase in the bubble generation frequency and decrease in the wall distance can be enhanced $\overline{vv}$. It is noteworthy that a local minimum exists for $\overline{vv}$. In the vicinity of the wall, before reaching its peak, $\overline{vv}$ did not exhibit an increasing trend with x/r_{eq} like $\overline{uu}$; instead, it initially decreased before eventually rising again after reaching a minimum value. An increase in bubble frequency accentuates this minimum. The distribution of the Reynolds shear stress is illustrated in Fig. 8 (c) and (f), with a positive or negative sign denoting the force direction. The shear stress
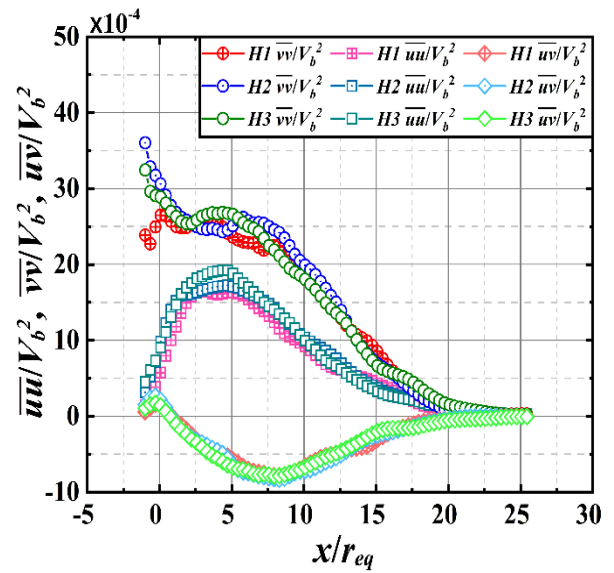
Fig. 9 Distribution of Reynolds Stress at Different Heights in the Flow Field. Initial wall distance: *L1*; Bubble generation frequency: *F1*

exhibited peak values in both the positive and negative directions. When the bubble generation frequencies were *F1* and *F2*, the negative peak value of the Reynolds shear stress surpassed the positive peak value. However, for the bubble generation frequency *F3*, the positive peak value of the Reynolds stress significantly exceeded the negative peak value.

The distribution of Reynolds stress at different heights in the flow field is shown in Fig. 9. The Reynolds stress is normalized to the bubble velocity (V_b). $\overline{uu}$ where represents the Reynolds normal stress in the flow direction, $\overline{vv}$ represents the Reynolds normal stress in the wall-normal direction, and $\overline{uv}$ represents the Reynolds shear stress. The initial wall distance is *L1*, and the bubble generation frequency is *F1*. The distribution patterns of $\overline{uv}$ and $\overline{uu}$ at different heights in the flow field are essentially identical. The peak value of $\overline{uu}$ increases slightly with height. Although there were overall similarities in the distribution laws of $\overline{vv}$ at different heights, noticeable differences occurred when x/r_{eq} < 2. Specifically, $\overline{vv}$ initially increases and then decreases at *H1*, whereas it decreases with x/r_{eq} for *H2* and *H3* and $\overline{vv}$ appears to be smaller at *H3* than at the other heights.

The distribution of the average turbulence intensities at different transverse positions in the flow field is shown in Fig. 10. *Tu* represents the total turbulence intensity, whereas Tu_u and Tu_v denote the components of the turbulence intensity along the flow- and wall-normal directions, respectively. The initial wall distance is *L1*. In Fig. 10 (a) and (d), the horizontal position is labeled *T1*; in Fig. 10 (b) and (e), it is labeled *T2*; and in Fig. 10 (c) and (f), it is labeled *T3*. The distances between these positions and the walls are listed in Table 5.
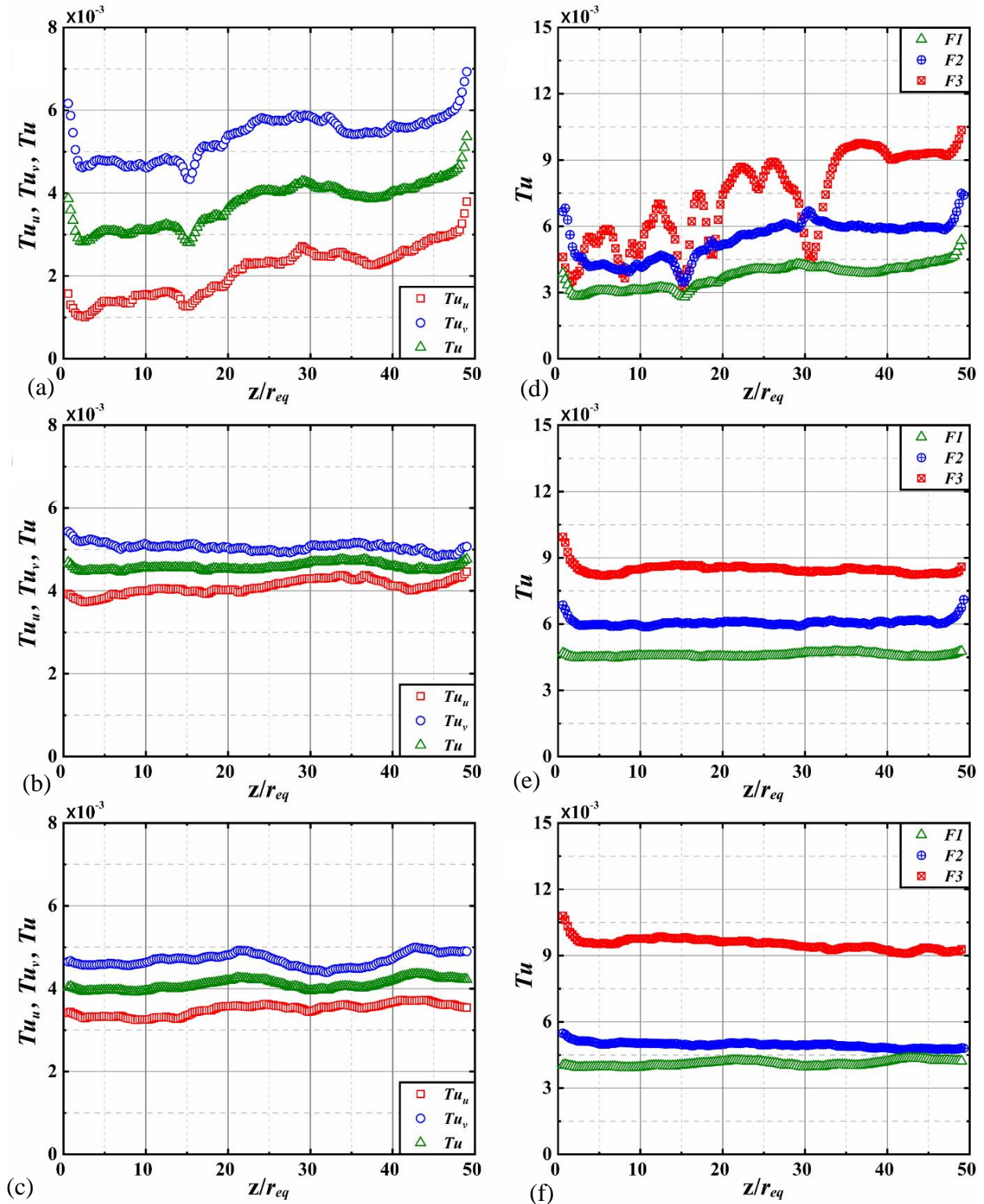
Fig. 10 Distribution of turbulence intensity at different transverse positions. (a) *F1*, *T1*; (b) *F1*, *T2*; (c) *F1*, *T3* ; (d) *T1* ; (e) *T2* ; (f) *T3*

Table 5 Vertical position within the bubbles induced flow field. *D* is the distance from a certain position in the flow field to the wall
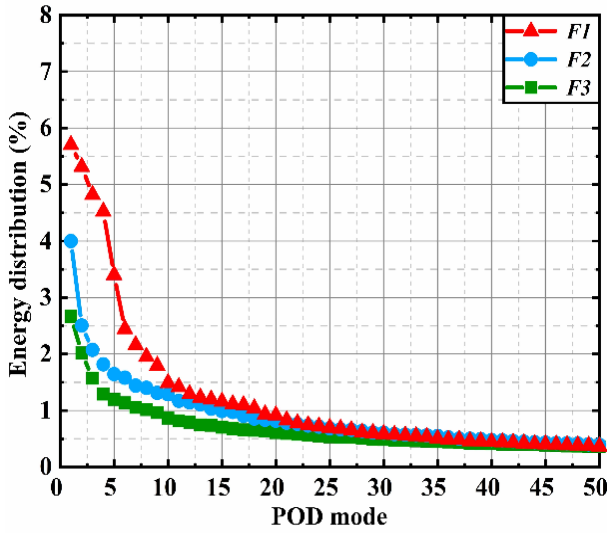
Position	*T1*	*T2*	*T3*
D/r_{eq}	0.1	1	2

The equation for computing turbulence intensity is expressed as follows:

$$Tu = \sqrt{\frac{(\overline{uu} + \overline{vv})}{2}} / U . \qquad (2)$$

The velocity pulsations in the flow- and wall-normal directions are represented by *u* and *v* respectively, and *U* denotes the average velocity of the flow field.

Fig. 11 Energy distribution of the induced flow field for bubbles with different generation frequencies. The energy level correlates with the distinct structures present in the flow field

The frequency of bubble generation shown in Fig. 10 (a)–(c) is *F1*. The distributions of Tu_u, Tu_v, and Tu are strongly correlated with their spatial locations. Similar distribution curves were observed at the same transverse positions, and Tu_u, Tu_v, and Tu exhibited approximate multiples. According to Fig. 10 (d)–(f), an increase in the bubble generation frequency led to higher turbulence levels. The turbulence distribution in low-frequency bubble-induced flow fields exhibited greater stability owing to the enhanced bubble-inducing ability caused by higher generation frequencies. Additionally, the changes in the turbulence intensity near the wall (*H1*) exhibited greater complexity. With an increase in the bubble frequency, more extreme turbulence value points appeared. In particular, when the frequency reached *F3*, there was a quasi-periodic fluctuation in the turbulence intensity with increasing height. This demonstrates that the walls can promote high-frequency bubble-induced flow fields to a certain extent.

Proper orthogonal decomposition (POD) is a powerful tool for analyzing complex flow fields with high accuracy and efficiency, making it an indispensable technique in the field of fluid mechanics (Wen et al., 2020). The velocity-time series of the bubble-induced flow field was decomposed using this method, and the dominant structure of the flow field was extracted through proper snapshot orthogonal decomposition (POD). The decomposition can be written as

$$u(X,t) = \sum_{i=1}^{N} \theta_i(t)\psi_i(X),\qquad(3)$$

where Ψ_i represents the characteristic mode of the ith order mode, $\theta_i(t)$ denotes the modal time coefficient representing temporal dynamics, and N is the total number of modes in the set.

The energy distribution of the induced flow field for the bubbles with different generation frequencies is shown

in Fig. 11. The energies of the different modes represent their respective contributions to the total kinetic energy of the entire flow field, reflecting the relative proportion of energy contained in each mode compared with the total energy. This can be calculated using the following equation:

$$E_i = \left\langle |a_i(t)|^2 \right\rangle_t, E_{total} = \sum_{i=1}^{N} E_i, P_i = \frac{E_i}{E_{total}} \times 100\% . \quad (4)$$

In the formula, E_i represents the energy possessed by the *i*-th mode, $a_i(t)$ represents the time coefficient of the *i*-th mode, E_{total} represents the total energy, P_i represents the proportion of energy, and $<\bullet>_t$ denotes time averaging.

The eigenvalue of the Proper Orthogonal Decomposition (POD) mode exhibits a rapid decay as the mode order increases, followed by a gradual decrease until it stabilizes. In POD, the higher-energy lower modes correspond to larger structures, whereas the lower-energy higher modes correspond to smaller structures. A greater eigenvalue signifies a higher energy content carried by a particular mode. The contribution of energy from higher-order modes is relatively low and negligible. Compared with *F1*, *F2*, and *F3* which have higher frequencies, a reduced proportion of energy is concentrated in the initial few modes. This observation suggests that an increase in bubble frequency leads to a more uniform scale distribution within the induced flow field.

The velocity fields of the first six orders obtained through Proper Orthogonal Decomposition (POD) analysis of the bubble-induced flow field are shown in Fig. 12. The frequency of bubble generation was *F3*. Mode 1, which has the highest energy content, is depicted in Fig. 12 (a), where symmetrical inverse vortex pairs are present in the wake, and no vortex shedding occurs. Fig. 12(b)–(e) show the results for Modes 2–5, respectively. As the mode order increased, vortex shedding became evident and exhibited clear periodicity, whereas the symmetric structure observed in the first mode disappeared. Additionally, the size of vortex shedding gradually decreases in higher-order modes because of the reduced energy carried by these modes. When the sixth-order mode was reached, there was no longer a clear vortex shedding periodicity.

The first-order velocity field obtained through POD of the bubble-induced flow field with varying generation frequencies is shown in Fig. 13. The bubble generation frequencies in Figs. 13 (a)–(c) correspond to *F3*–*F1*. As the generation frequency decreased, the bubble-induced flow field exhibited alternating vortex shedding akin to that observed in the higher-order mode, as illustrated in Fig. 12. Reducing the frequency advances the onset of vortex shedding across the different modes. In a high-frequency bubble-induced flow field, bubbles possess an enhanced ability to induce flow, resulting in an increased flow field induced by subsequent bubbles. However, these bubbles disrupt the structure of the preceding bubble-induced flow field. Consequently, compared with the lower-frequency cases, higher-frequency bubbling leads to a more uniform energy distribution within the induced flow field and a more continuous order of vortex shedding.
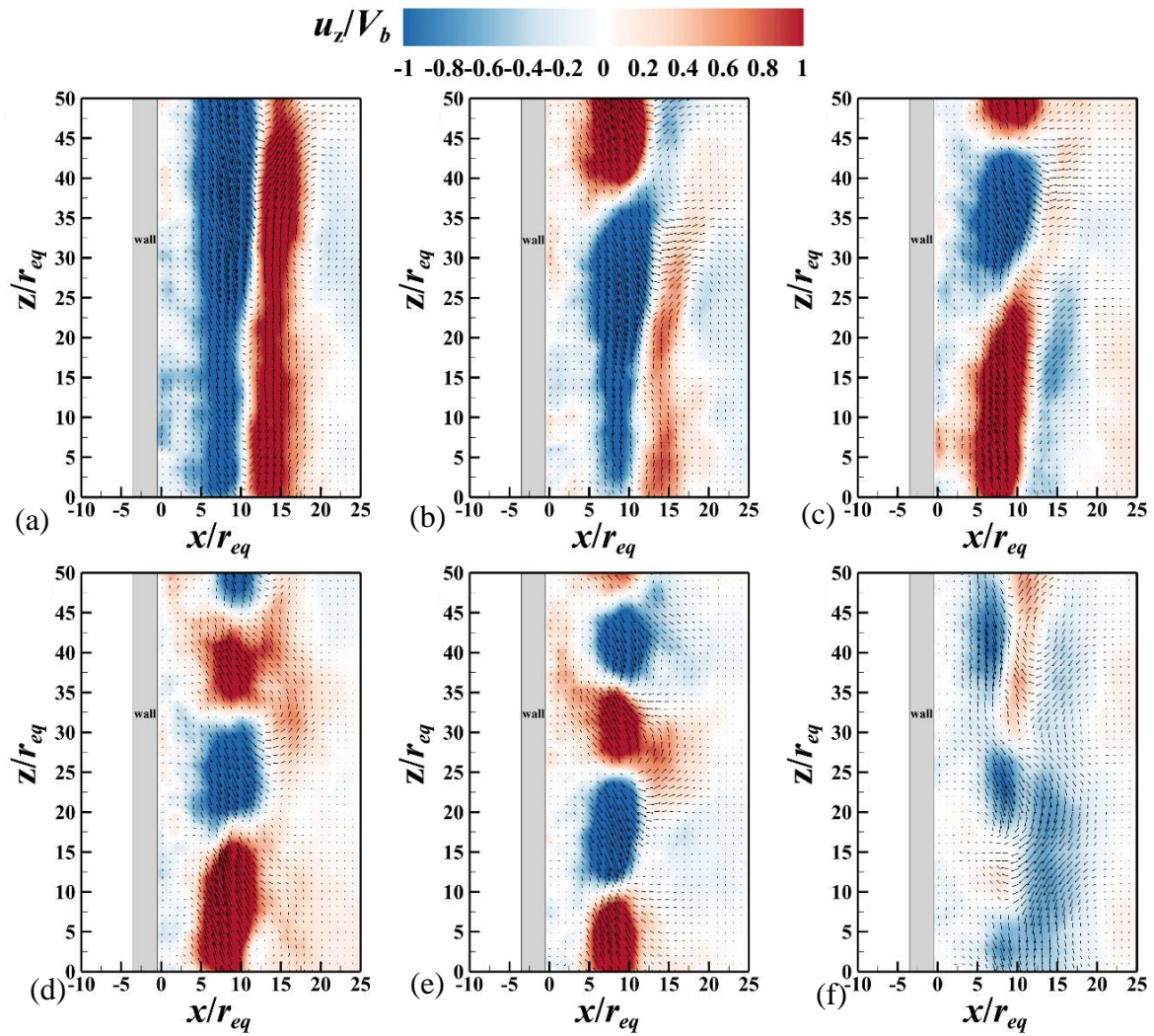
Fig. 12 Velocity fields of the first six orders obtained through proper orthogonal decomposition (POD) analysis for the bubble-induced flow field
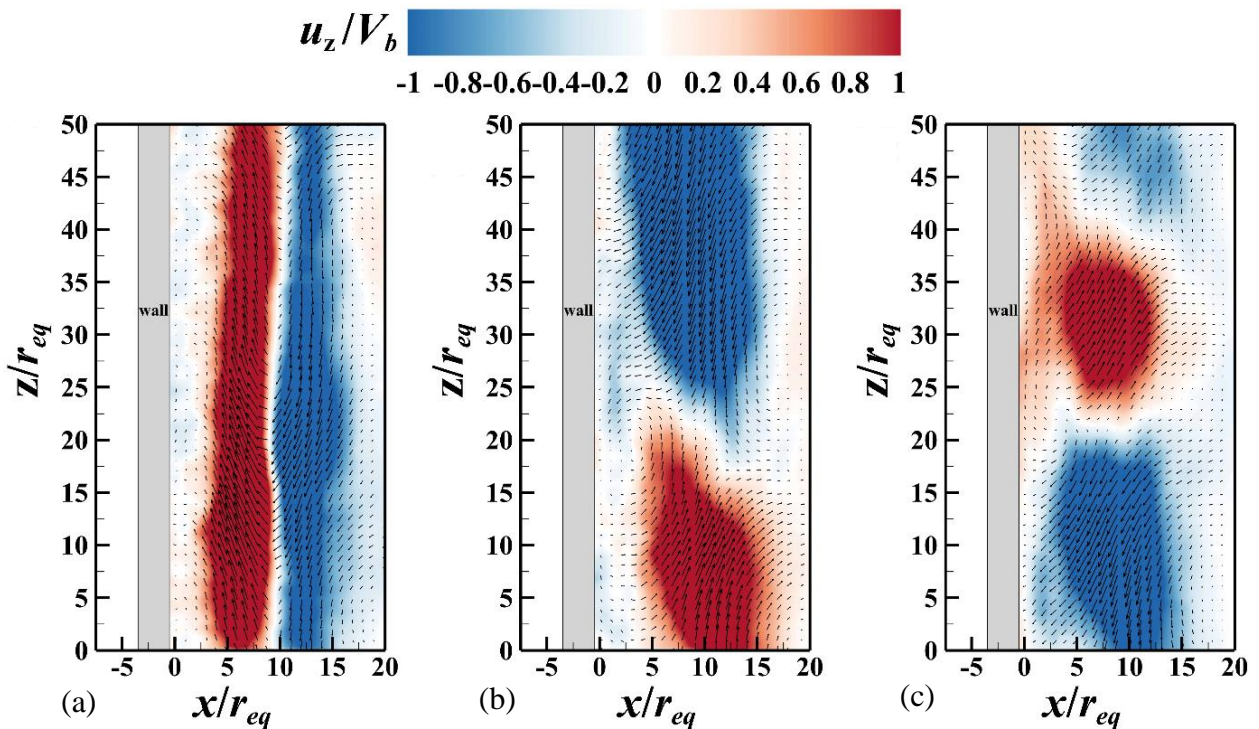

Fig. 13 First-order velocity field obtained through POD decomposition of the bubble-induced flow field with varying generation frequencies. (a) *F3*; (b) *F2*; (c) *F1*

4. CONCLUSION

This study conducted an experimental investigation into the behavior of bubbles in a quiescent liquid near a vertical wall, with a particular focus on the induced flow field characteristics. The dynamics of bubble chains and their induced flow were meticulously recorded using shadow imaging and Particle Image Velocimetry (PIV). Additionally, the research examined the influence of bubble generation frequency and the initial distance from the wall on the velocity distribution of the bubbles and the resulting flow field. The main findings from this work are as follows:

(1) The presence of a wall exerted a dual effect on the motion of the bubble chain, impeding and enhancing its movement. This inhibitory effect diminished with increasing distance from the wall and could be mitigated by increasing the bubble generation frequency.

(2) The flow field induced near the wall produces secondary vortices. These vortices arise from the interplay between the influence of the wall and the accumulation of leading-edge vortices shed by the bubbles in contact with the wall, a phenomenon that is particularly pronounced at medium and low generation frequencies.

(3) At high generation frequencies, the formation of secondary vortices cannot be ascribed solely to the aforementioned factors. Instead, their emergence was predominantly the result of secondary induction effects within the bubble-induced flow, with the wall's primary role being to compress the flow field.

(4) The Proper Orthogonal Decomposition (POD) analysis demonstrates that the evolution of vortex structures across various scales is closely correlated with the bubble generation frequency, where a higher frequency leads to a more uniform energy distribution.

ACKNOWLEDGEMENTS

CONFLICT OF INTEREST

The authors declare no competing financial interest.

AUTHORS CONTRIBUTION

Runze Cai: Methodology, Investigation, Data curation, Writing - Original draft preparation. **Jiao Sun:** Validation, Supervision, Writing - Reviewing and Editing. **Wenyi Chen:** Conceptualization, Supervision, Project administration.

REFERENCES

Cai, R., Sun, J., & Chen, W. (2024). Near-wall bubble migration and wake structure in viscous liquids. *Chemical Engineering Research and Design*, *202*, 414-428. https://doi.org/10.1016/j.cherd.2024.01.007

Celata, G. P., D'Annibale, F., Di Marco, P., Memoli, G., & Tomiyama, A. (2007). Measurements of rising velocity of a small bubble in a stagnant fluid in one- and two-component systems. *Experimental Thermal and Fluid Science*, *31*(6), 609-623. https://doi.org/10.1016/j.expthermflusci.2006.06.006

Chen, Y., Tu, C., Yang, Q., Wang, Y., & Bao, F. (2021). Dynamic behavior of a deformable bubble rising near a vertical wire-mesh in the quiescent water. *Experimental Thermal Fluid Science*, *120,* 110235. https://doi.org/10.1016/j.expthermflusci.2020.110235

Choi, H., Lee, J., & Park, H. (2019). Wake structures behind a rotor with superhydrophobic-coated blades at low Reynolds number. *Physics of Fluids*, *31*(1), 015102. https://doi.org/10.1063/1.5054039

Dai, B., Cao, Y., Zhou, X., Liu, S., Fu, R., Li, C., & Wang, D. (2024a). Exergy, carbon footprint and cost lifecycle evaluation of cascade mechanical subcooling CO2 commercial refrigeration system in China. *Journal of Cleaner Production*, *434*, 140186. https://doi.org/10.1016/j.jclepro.2023.140186

Dai, B., Wang, Q., Liu, S., Zhang, J., Wang, Y., Kong, Z., Wang, D. (2024b). Multi-objective optimization analysis of combined heating and cooling transcritical CO2 system integrated with mechanical subcooling utilizing hydrocarbon mixture based on machine learning. *Energy Conversion Management*, *301*, 118057. https://doi.org/10.1016/j.enconman.2023.118057

Dai, B., Wu, T., Liu, S., Qi, H., Zhang, P., Wang, D., & Wang, X. (2024c). Flow boiling heat transfer characteristics of zeotropic mixture CO2/R152a with large temperature glide in a 2 mm horizontal tube. *International Journal of Heat Mass Transfer*, *218*, 124779. https://doi.org/10.1016/j.ijheatmasstransfer.2023.124779

de Vries, A. W. G. (2001). *Path and wake of a rising bubble*. University of Twente. Enschede, The Netherlands.

de Vries, A. W. G., Biesheuvel, A., & Wijngaarden, L. v. (2002). Notes on the path and wake of a gas bubble rising in pure water. *International Journal of Multiphase Flow*, *28*(11), 1823-1835. https://doi.org/10.1016/S0301-9322(02)00036-8

Gong, Z., Cai, J., & Lu, Q. (2020). Experiment characterization of the influence of wall wettability and inclination angle on bubble rising process using PIV. *European Journal of Mechanics / B Fluids*, *81*, 62-75. https://doi.org/10.1016/j.euromechflu.2020.01.005

Jeong, H., & Park, H. (2015). Near-wall rising behaviour of a deformable bubble at high Reynolds number. *Journal of Fluid Mechanics*, *771*, 564-594. https://doi.org/10.1017/jfm.2015.191

Khodayar, J., & Davoudian, S. H. (2018). Surface wettability effect on the rising of a bubble attached to a vertical wall. *International Journal of Multiphase Flow*, *109*, 178–190. https://doi.org/10.1016/j.ijmultiphaseflow.2018.06.015

Krishna, R., Urseanu, M. I., Baten, J. M. V., & Ellenberger, J. (1999). Wall effects on the rise of single gas bubbles in liquids. *International Communications in Heat Mass Transfer*, *26*(6), 781-790. https://doi.org/10.1016/S0735-1933(99)00066-4

Lee, J. H., Kim, H., Lee, J., & Park, H. (2021). Scale-wise analysis of upward turbulent bubbly flows: An experimental study. *Physics of Fluids*, *33*, 053316. https://doi.org/10.1063/5.0048199

Lee, J., & Park, H. (2017). Wake structures behind an oscillating bubble rising close to a vertical wall. *International Journal of Multiphase Flow*, *91*, 225-242. https://doi.org/10.1016/j.ijmultiphaseflow.2017.02.004

Lee, J., & Park, H. (2022). Flow induced by the single-bubble chain depending on the bubble release frequency. *Physics of Fluids*, *34, 033312*. https://doi.org/10.1063/5.0083281

Li, S. Y., Xu, Y., & Wang, J. J. (2021). Characteristics and flow dynamics of bubble-in-chain rising in a quiescent fluid. *International Journal of Multiphase Flow*, *143*, 103760. https://doi.org/10.1016/j.ijmultiphaseflow.2021.103760

Maeng, H., & Park, H. (2021). An experimental study on the heat transfer by a single bubble wake rising near a vertical heated wall. *International Journal of Heat Mass Transfer*, *165*, 120590. https://doi.org/10.1016/j.ijheatmasstransfer.2020.120590

Métrailler, D., Reboux, S., & Lakehal, D. (2017). Near-wall turbulence-bubbles interactions in a channel flow at Re τ = 400: A DNS investigation. *Nuclear Engineering and Design*, *3213*, 180-189. https://doi.org/10.1016/j.nucengdes.2016.10.055

Mougin, G., & Magnaudet, J. (2002). Path instability of a rising bubble. *Physical Review Letters*, *88*(1), 014502. https://doi.org/10.1103/PhysRevLett.88.014502

Sanada, T., Watanabe, M., Fukano, T., & Kariyasaki, A. (2005). Behavior of a single coherent gas bubble chain and surrounding liquid jet flow structure. *Chemical Engineering Science*, *60*(17), 4886-4900. https://doi.org/10.1016/j.ces.2005.04.010

Sugioka, K. I., & Tsukada, T. (2015). Direct numerical simulations of drag and lift forces acting on a spherical bubble near a plane wall. *International Journal of Multiphase Flow*, *71*, 32-37. https://doi.org/10.1016/j.ijmultiphaseflow.2014.12.001

Wang, B. B., & Socolofsky, S. A. (2019). Characteristics of mean flow and turbulence in bubble-in-chain induced flows. *Physical Review Fluids*, *4*(5). https://doi.org/10.1103/PhysRevFluids.4.054302

Wen, X., Liu, J., Li, Z., Peng, D., Zhou, W., Kim, K. C., & Liu, Y. (2020). Jet impingement using an adjustable spreading-angle sweeping jet. *Aerospace Science Technology*, *105*, 105956. https://doi.org/10.1016/j.ast.2020.105956

Yan, H. J., Zhang, H. Y., Zhang, H. M., Liao, Y. X., & Liu, L. (2023). Three-dimensional dynamics of a single bubble rising near a vertical wall:Paths and wakes. *Petroleum Science*, *20*(3), 1874-1884. https://doi.org/10.1016/j.petsci.2023.02.014

Yan, H., Zhang, H., Liao, Y., Zhang, H., Zhou, P., & Liu, L. (2022). A single bubble rising in the vicinity of a vertical wall: A numerical study based on volume of fluid method. *Ocean Engineering*, *263*, 112379. https://doi.org/10.1016/j.oceaneng.2022.112379

Yin, J., Zhang, Y., Zhu, J., Lv, L., & Tian, L. (2021). An experimental and numerical study on the dynamical behaviors of the rebound cavitation bubble near the solid wall. *International Journal of Heat Mass Transfer*, *177*(10), 121525. https://doi.org/10.1016/j.ijheatmasstransfer.2021.121525

Yu, Q., Ma, X., Wang, G., Zhao, J., & Wang, D. (2020). Thermodynamic Effect of Single Bubble Near a Rigid Wall. *Ultrasonics Sonochemistry*, *105396*. https://doi.org/10.1016/j.ultsonch.2020.105396

Yuan, J., Weng, Z., & Shan, Y. (2021). Modelling of double bubbles coalescence behavior on different wettability walls using LBM method. *International Journal of Thermal Sciences*, *168*, 107037. https://doi.org/10.1016/j.ijthermalsci.2021.107037

Zaruba, A., Lucas, D., Prasser, H.-M., & Höhne, T. (2007). Bubble-wall interactions in a vertical gas–liquid flow: Bouncing, sliding and bubble deformations. *Chemical Engineering Science*, *62*(6), 1591-1605. https://doi.org/10.1016/j.ces.2006.11.044

Zenit, R., & Magnaudet, J. (2008). Path instability of rising spheroidal air bubbles: A shape-controlled process. *Physics of Fluids*, *20*(6), 061702. https://doi.org/10.1063/1.2940368

Zhang, J., & Ni, M. J. (2017). What happens to the vortex structures when the rising bubble transits from zigzag to spiral? *Journal of Fluid Mechanics*, *828*, 353-373. https://doi.org/10.1017/jfm.2017.514

Zhang, Y., Dabiri, S., Chen, K., & You, Y. (2020). An initially spherical bubble rising near a vertical wall. *International Journal of Heat Fluid Flow*, *85*, 108649. https://doi.org/10.1016/j.ijheatfluidflow.2020.108649